

## CLASSIFICATION AND INVESTIGATION OF RECOMBINATION ACTIVE DEFECT STRUCTURES IN MULTICRYSTALLINE SILICON SOLAR-CELLS

D. Lausch<sup>1</sup>, K. Petter<sup>2</sup>, R. Bakowskie<sup>2</sup>, J. Bauer<sup>3</sup>, O. Breitenstein<sup>3</sup>, C. Hagendorf<sup>1</sup>

<sup>1</sup>Fraunhofer-Center für Silizium-Photovoltaik CSP, Walter-Hülse-Straße 1, 06120 Halle (Saale), Germany

<sup>2</sup>Q-Cells SE, Sonnenallee 17-21, 06766 Bitterfeld-Wolfen, Germany

<sup>3</sup>Max Planck Institute of Microstructure Physics, Weinberg 2, 06120 Halle (Saale), Germany

**ABSTRACT:** In this contribution two models explaining the recombination behavior of the different defect types introduced in a previous publication are discussed. For this we have applied detailed microscopic investigations, temperature-dependent EBIC measurements and root cause analysis on the nm-scale. We could separate the large amount of recombination active defects into four different classes: type-A<sub>P</sub>, type-A<sub>G</sub>, type-B and type-C. It was shown that iron precipitates are responsible for the recombination behavior at type-A<sub>P</sub> sites leading to an interface recombination. At type-A<sub>G</sub> regions, most likely decorated with iron impurities, deep defect states E<sub>M</sub> are responsible for the recombination behavior and can be described by the model of Kveder *et al.* The recombination processes at Type-B defect structures are either due to a low impurity level or a shallower position of the defect level E<sub>M</sub> both explaining the observed high intensity of defect luminescence. It is concluded that the recombination process at type-C defects is similar to type-A<sub>G</sub> defect structures. The temperature dependency of the recombination behavior is in good agreement with the model described by Kveder *et al.* for all defect types.

**Keywords:** defect classification, recombination active defects, metal contamination, silicon solar cells, recombination model of Kveder

### 1 INTRODUCTION

Currently, the main challenges of the photovoltaic industry are to reduce the costs per watt peak and to increase the durability of the solar modules. To reduce the costs a considerable way is to use multicrystalline silicon (mc-Si) wafers made from electronic grade (eg-Si) or even upgraded metallurgical grade (umg-Si) silicon feedstock. However, the solar cell efficiency of solar cells made of mc-Si wafers is lower compared to solar cells made of monocrystalline silicon wafers. A major reason for this is the presence of different recombination active defect structures in mc-Si materials. These defect structures have an influence on (i) the solar-cell efficiency and (ii) the electrical breakdown behavior hence the reliability of the solar module. Therefore it is of utmost importance to understand the cause and the physical mechanisms of recombination and prebreakdown processes at these defect structures. For a thorough analysis of the large amount of these defects, it is necessary to classify the defect structures to investigate the causes and mechanism of each class separately. An important requirement for this classification is a simple and industry-related application. The knowledge obtained by sophisticated and detailed investigations can be reversibly interconnected to the classification on industrial level. Therefore costly methods and time-consuming investigations can be avoided.

In a previous publication [1] we have introduced such a classification of recombination active defect structures in mc-Si solar cells by means of the recombination and prebreakdown behavior based on a procedure published by Bothe *et al.* [2]. The prebreakdown behavior of mc-Si solar cells is described in [3]. In this contribution we always discuss the type-2 prebreakdown sites [4, 5] which are always located at positions with high recombination activity. In this paper it will be shown that not all recombination active defect structures show type-2 prebreakdown behavior; only so called type-A defect structures.

In summary we could clearly separate two different types of recombination active defects denoted as type-A and type-B on a macroscopic scale. It was shown that the

same classification scheme can be transferred to the microscopic scale allowing classifying every defect separately providing a base for a root cause analysis. Nevertheless, we had to introduce a third type-C. Based on this classification we could observe the following attributes.

Type-A defects are characterized by:

- very low band-to-band luminescence and lifetime [1]
- no defect luminescence between 0.72-0.85 eV [1]
- prebreakdown behavior of type-2 [1]
- detrimental impact on solar cell efficiency; correlation of area fraction of type-A defects and open-circuit voltage V<sub>oc</sub> [7]
- Partly activation of type-A defects by the solar cell process [7] and temperature treatment only [8]

Type-B defect structures are characterized by:










- slightly reduced band-to-band luminescence and lifetime [1]
- high intensity of defect luminescence between 0.72-0.85 eV [1]
- no prebreakdown behavior of type-2 [1]

Type-C defects are characterized by:

- high recombination activity [1]
- no defect luminescence [1]
- no prebreakdown behavior of type-2 [1]

Additionally, we have shown that the introduced classification can also be applied to mc-Si solar cells made from umg-Si feedstock of quite different quality [3]. The main properties for classifying the defects are summarized as pictograms in Table 1.

In this contribution we will present two models describing the recombination processes taking place at the different defect types based on detailed microscopic and temperature dependent investigations.

	Recombination behavior	prebreakdown behavior	defect luminescence
	EL	ReBEL (type-2)	ELsub
Type A			
Type B			
Type C			

**Table 1:** Summary of the main properties of the defect classes as pictograms required for applying the classification of recombination active defects.

## 2 EXPERIMENTAL

The samples analyzed were standard screen printed mc-Si solar cells made from umg-Si and eg-Si feedstock produced in an industrial production line.

The lateral distribution of recombination active defects are localized by forward biased electroluminescence (EL) imaging [10] detecting the band-to-band luminescence, where highly recombination active regions appear dark. The spectrally integrated, spatially resolved electro-luminescence (EL) images were acquired at room temperature using a Si charge coupled device (CCD) camera. In order to detect the defect sub-band luminescence between 0.72-0.85 eV [11] this setup was equipped with an InGaAs CCD (ELsub). Regions with a high defect luminescence appear bright. Prebreakdown sites emit light under reverse bias which makes it possible to locate the exact positions of prebreakdown sites with high spatial resolution by using reverse-biased electroluminescence (ReBEL) with a Si CCD detector [12]. For investigations on a micrometer scale the corresponding CCD cameras were mounted onto an optical microscope.

The electron beam induced current (EBIC) measurements were acquired by means of a Hitachi SU70 SEM equipped with a Point Electronic EBIC system. Also here, recombination active defect structures are visible as dark contrast with high spatial resolution. Transmission electron microscopy images (TEM) were acquired using an FEI Tecnai.

## 3 RESULTS

### 3.1 Microscopic investigations of type-A defects

It was shown in [1] that both type-A and type-B defect structures can be identified on a microscopic scale. Therefore a classification of each defect separately is possible providing a base for further investigations. In Fig. 1 a type-A defect structure is shown in superior lateral resolution. Dark spots with increased recombination activity next to the defect can be seen (marked with arrows in Fig. 1). Note that these positions are not exactly at the grain boundary of the mc-Si material. The reason for this will be discussed later. The positions with increased recombination activity correlate quite well with type-2 prebreakdown sites visible by comparing the EBIC measurement in Fig. 1 (a) and the  $\mu$ -ReBEL measurement in Fig. 1(b). Nevertheless, the type-2 prebreakdown sites are exactly at the crystal defect within the lateral resolution of the used method. These positions will be denoted in the following as type- $A_P$ . The subscript P stands for precipitate since metal precipitates can be found at these positions as shown later.

In between these type- $A_P$  sites the line defect shows still a high recombination activity but no type-2 prebreakdown behavior. These regions are denoted as type- $A_G$  in the following. Here the subscript G stands for grain boundary.

Therefore type-A regions have to be separated on a microscopic scale into type- $A_P$  sites (having an increased spot like recombination and type-2 prebreakdown behavior) and type- $A_G$  lines (having high recombination activity along the line defect and lying in between type- $A_P$  sites).

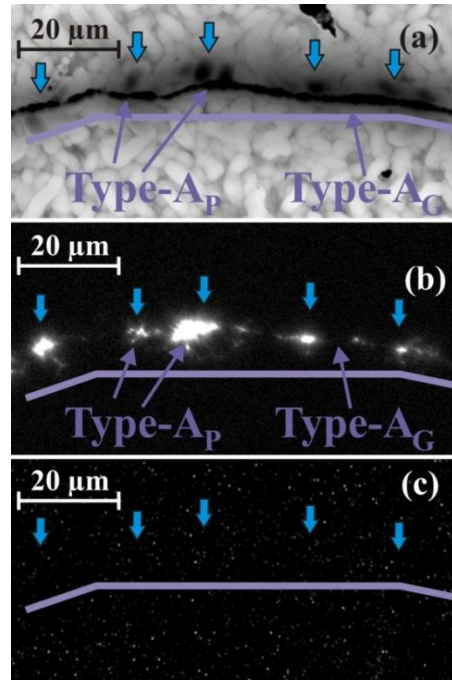


**Figure 1:** (a) EBIC, (b)  $\mu$ -ReBEL (type-2 prebreakdown) and (c)  $\mu$ -ELsub investigation of a sample taken out of a type-A region. Obviously, type-A defect structures have to be distinguished on a microscopic scale into type- $A_P$  sites (having an increased spot like recombination (a) and type-2 prebreakdown (b) behavior) and type- $A_G$  lines (having high recombination activity along the line defect and lying in between type- $A_P$  sites).

### 3.2 Temperature-dependent EBIC measurements

In order to discuss the physical mechanisms taking place at recombination active defect structures temperature-dependent EBIC measurements have been performed. The recombination behavior at room temperature detected by means of EBIC of a region with two type-A defect structures can be seen in Fig. 2(a). Also here the type- $A_P$  and type- $A_G$  defects can be easily separated. Additionally, a lot of non-recombination active defect structures can be found in this region visible due to their etch pits in a secondary electron image and marked with a black circle in Fig. 2(a) and (b). It should be mentioned here that only a minor number of the crystal defects show recombination activity at all. The EBIC measurement of the same region but at 90 K is shown in Fig. 2(b). Still, type- $A_P$  and type- $A_G$  defects are recombination active. In contrast to this the defect structures showing no recombination activity at room temperature are strong recombination active at 90 K.

To get a more quantitative insight into the temperature dependency of the recombination processes

at the different defect types the EBIC contrast behavior  $C_{\text{defect}}$  which is directly correlated to the recombination strength [13] was measured. The EBIC contrast  $C_{\text{defect}}$  is defined with the EBIC current  $I_{\text{defect}}$  exactly at the defect structure and  $I_0$  away from the defect structure to  $C_{\text{defect}} = (I_0 - I_{\text{defect}})/I_0$ . The temperature-dependent EBIC contrast  $C_{\text{defect}}$  of three prominent defect structures (a type- $A_G$ , a type-B and a non-recombination active defect structure) is shown in Fig. 2(c). The EBIC contrast  $C_{\text{defect}}$  of the type- $A_G$  defect structure is around 40% at room temperature. Starting from room temperature the type- $A_G$  defect structure is characterized by a slightly decreasing contrast behavior with decreasing temperature. The type-B defect show a much lower EBIC contrast  $C_{\text{defect}}$  of about 10% at room temperature. In contrast to the type- $A_G$  defect structure type-B structures show an increasing recombination behavior with decreasing temperature up to the EBIC contrast of the type- $A_G$  defect structure at around 120 K. Of course, the non-recombination active defect structures show no EBIC contrast at room temperature but become strongly recombination active below 140K. The strong scattering of our measurements are most likely due to the influence of the surface morphology on the EBIC measurement since the solar cells have a textured and therefore rough surface. Similar results have already been observed and discussed for single dislocations in n-type monocrystalline silicon material by Kittler *et al.* [14].

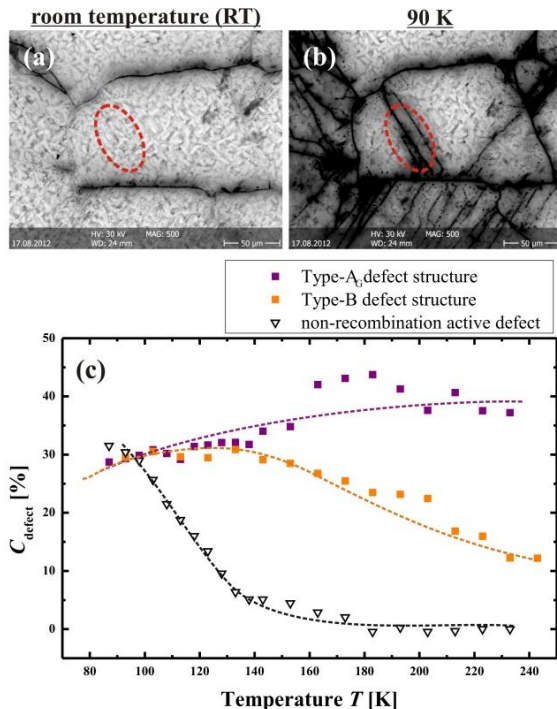


**Figure 2:** EBIC investigation of a region having type-A defects at room temperature (a) and at 90K (b). Few examples for non-recombination active defects are marked with a red circle. The non-active defect structures show a strong recombination behavior below 140 K. The type-A defects are strong recombination active at room temperature as well as at 90 K. The EBIC contrast  $C_{\text{defect}}$  of a type-A, a type-B and a non-recombination active defect depending on the temperature is shown in (c). The dashed lines show the trends described by the Kveder model described in Sec. 4.

### 3.3 Root cause analysis of the defect types

The defect classification recovered at microscopic level enables starting a root cause analysis. As discussed in section 3.1 type-A defects have to be distinguished into type- $A_P$  (having an increased spot like recombination and type-2 prebreakdown behavior) and type- $A_G$  (having high recombination activity along the line defect; no type-2 prebreakdown behavior can be observed).

Since at type- $A_P$  defect structures always a type-2 prebreakdown occur, we use this behavior to apply a root cause analysis. We show in [5] that the type-2 prebreakdown is caused by small  $\alpha$ -FeSi<sub>2</sub> rods having a diameter of around 30 nm. For a more detailed discussion about the preparation and investigation of type-2 prebreakdown sites and the prebreakdown model it is referred to [5] and [16]. In Fig. 3(a) a type- $A_P$  defect type at a large angle grain boundary is shown. At the transmission electron microscopy (TEM) image of a TEM exactly at the position of the type- $A_P$  defect site lamella in Fig. 2(b) the rod-like nature of the inclusion can be seen. A spot electron dispersive x-ray (EDX) mapping of a small region marked with a white rectangle in Fig. 2(b) reveal the chemical composition of the detected precipitate. The obtained rod obviously consists of iron (Fig. 2(c)). The silicon signal visible in Fig. 2(d) at this position is increasing to the interface of silicon and iron underlying the rod-like nature. Therefore it is reasonable that the recombination process at type- $A_P$  defects is caused by this metal precipitate. This also would justify the point-like nature of the increased recombination behavior at the type- $A_P$  defect structures next to the crystal defect as discussed later.

We have shown in [7] and [8] that the type-A defect structures are activated due to temperature treatment. Therefore it can be assumed that the regions in between the type  $A_P$  sites (denoted as type- $A_G$ ) are highly contaminated by iron impurities released at high temperatures from the iron precipitates introducing defect levels into the forbidden band gap of the silicon material. This assumption is supported by the temperature-dependent EBIC measurements at type- $A_G$  structures and the Kveder model as discussed later.

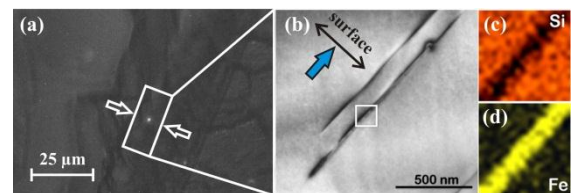


**Figure 3:** (a)  $\mu$ -ReBEL image of a type-2 prebreakdown site visible as a bright spot. Exactly at this position a TEM lamella has been prepared (b). The precipitates are visible as darker lines. The element concentration of a small region marked with a white rectangle is shown for silicon in (c) and for iron in (d).

Also a type-B defect structure showing defect luminescence and recombination activity was chosen for a root cause analysis. Since the defect luminescence within our resolution seems to be homogeneously distributed along the line defect, we have chosen a random position. Unfortunately, the spot EDX measurements at a lamella prepared at the line defect did not reveal any evident indication on a possible cause (not shown here). Bothe *et al.* [2] have discussed the influence of oxygen at these positions. However, we could not observe a correlation of oxygen with type-B defect structures. In particular, we have measured the interstitial

oxygen concentration  $O_i$  over the brick height showing a decreasing concentration from bottom to top. In contrast to this the ELsub intensity integrated over the whole wafer is increasing from bottom to the top of the brick. Nevertheless the cause for the defect luminescence is unclear so far and currently under discussion. But a micrometer scaled impurity causing the type-B behavior can be excluded. A possible influence of the anti-reflection coating formation was discussed recently [9].

#### 4 DISCUSSION AND PHYSICAL MODEL

##### 4.1 Interface recombination at type- $A_p$ defects

As it is shown in section 3.3 the recombination behavior for Type- $A_p$  defect structures is caused by metal precipitates. It can be assumed that the interface between silicon and the metal precipitate provide a large number of interface states. Therefore, the generated electron-hole pairs will recombine at these interface states between the silicon and the metal precipitate as shown schematically in Fig. 4. Hence the recombination process at type- $A_p$  defects can be explained by interface recombination which can be considered as a special case of the Shockley-Read-Hall recombination [17,18] with a continuous distribution of defect levels instead of a single defect level in the band gap. The recombination rate  $R$  for electron-hole pairs at these interface states is quite high. Thus, the thermal velocity of the charge carriers  $v_{th}$  describes the upper limit of the interface recombination velocity ( $S_{max} \sim 10^7$  cm/s) [19]. This would explain the strong recombination activity and the missing defect luminescence. The type-2 prebreakdown behavior at type- $A_p$  sites is explained elsewhere [5].

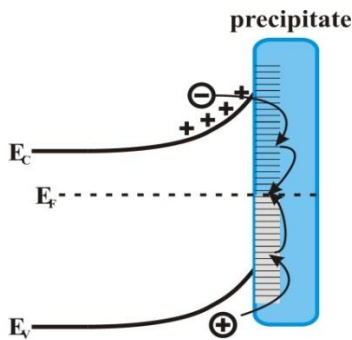


**Figure 4:** Schematic illustration of the band structure and interface recombination at the metal precipitate. The recombination of the minority carriers take place via the interface states at the interface between the precipitate and the silicon material.

The rod-like nature of the metal precipitates can explain the spot-like occurrence of increased recombination activity next to the grain boundary visible in Fig. 1(a) and Fig. 5(a). It should be mentioned that the type- $A_p$  sites can also be located exactly at the grain boundary. This behavior is caused by the geometrical position of the grain boundary in the bulk material. As it can be seen in the TEM image in Fig. 5(b), this line defect is not perpendicular to the surface. Here the line defect is visible as a darker line starting at the bottom of the etch pit. The direction of the defect line is visualized by a red arrow. Since the metal precipitate is laying in the grain boundary the metal precipitate is also located angled in the bulk material. Therefore, the main influence

of the precipitate must not be exactly at the puncture point of the line defect with the surface. If the defect line is perpendicular to the wafer surface the type- $A_p$  regions would be visible by means of EBIC exactly around the defect line.

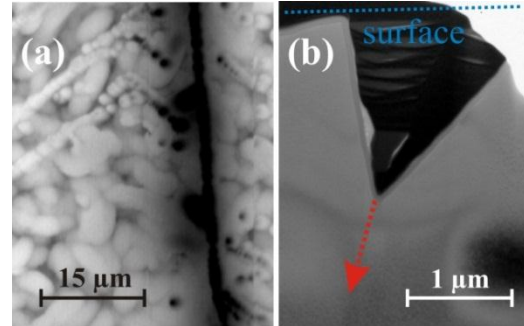


**Figure 5:** (a) EBIC measurement of type-A defect structure. The influence of the metal precipitate can be seen as spot-like regions with increased recombination activity (type- $A_p$ ). A similar grain boundary is shown in the cross section in (b). Here the direction of the defect line is marked with a red arrow.

##### 4.2 The recombination model of Kveder

The Kveder model [15] is a statistical model that allows a quantitative description of the recombination of minority carriers at dislocation lines under EBIC conditions. A peculiarity of this model is the consideration of a deep defect state with an energy  $E_M$  below the conduction band, their interaction with shallow defect bands  $D_e$  and  $D_h$  introduced by the inhomogeneity of the crystal structure and their temperature description. The total recombination rate  $R_T$  of the minority carriers at the dislocation is the sum of the rates of the single recombination processes visualized by arrows in Fig. 6. Despite the fact that the Kveder model is describing the recombination process at a single dislocation, we will show that a qualitative description of the recombination processes at the investigated grain boundaries is possible. The recombination process at type- $A_G$ , type-B and type-C defects can be explained by the Kveder recombination model as follows:

##### Type- $A_G$ defect structures:

Since type- $A_G$  defects occur in between of type- $A_p$  sites and are partly activated due to temperature processes we assume a high contamination with iron impurities of type- $A_G$ . These iron impurities are introducing many deep defect levels in the band gap. These defect levels are idealized in our model as one deep defect level  $E_M$  having different characteristic depending on the type of impurity and its concentration.

Based on the results of the Kveder model a defect with energy  $E_M \sim 0.5$  eV and high concentration  $N_M$  shows a high EBIC contrast  $C_{defect}$  at room temperature and a slightly decreasing recombination activity with decreasing temperature over the whole temperature range. This coincides quite well with our temperature measurements in Fig. 2(c). The trend described by the Kveder model is visualized as a purple dotted line in Fig. 2(c). The temperature-dependent EBIC measurement confirm our assumption of a high decoration of type- $A_G$  defects with iron since the EBIC contrast  $C_{defect}$  follows the trend predicted by Kveder for a highly contaminated defect structure.

The strong recombination via the deep defect level  $E_M$  can explain the observed characteristics of type- $A_G$  defects, e.g. the detrimental impact on the solar cell performance and the missing defect luminescence between 0.72-0.85 eV.

#### Type-B defect structures:

At room temperature type-B defects show a low EBIC contrast compared to type- $A_G$  defect structures. With decreasing temperature type-B defects show an increasing recombination activity up to a level of the type-A defect. This behavior is in good agreement with the Kveder model for a line defect with either (i) a lower concentration  $N_M^*$  of deep level impurities or (ii) a shallower defect level ( $E_M^* \sim 0.2$  eV to 0.3 eV). In both cases the observed defect luminescence can be explained either (i) by an increased recombination via the shallow defect bands  $D_e$  and  $D_h$  or (ii) by a recombination via the defect level  $E_M^* \sim 0.3$  eV within the band gap. In both cases the emitted radiation can be detected by the InGaAs CCD. With decreasing temperature the recombination probability via the shallow defect bands  $D_e$  and  $D_h$  become more probable leading to an increased recombination strength as visible in Fig. 2(c). The trend predicted by the Kveder model is depicted with a yellow dashed line.

The described recombination process at type-B defects can explain the high intensity of the defect luminescence and the lower recombination activity compared to type-A defects.

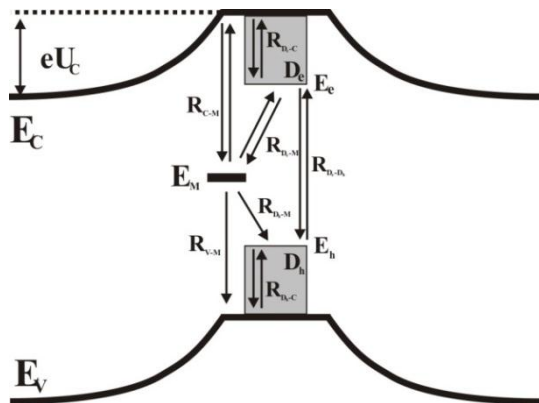


**Figure 8:** Schematic illustration of the band diagram described by Kveder et al. The possible recombination paths of the minority carriers are shown as arrows.

#### Type-C defect structures:

Based on the strong recombination activity, the missing defect luminescence and prebreakdown behavior of type-2 and according to our model we assume that the situation at type-C line defects is similar to type- $A_G$ . Therefore, deep levels  $E_M$  within the band gap introduced by impurities are present but without type- $A_P$  sites with precipitates in the vicinity of type-C line defects. Since the causes and possible impurities are unclear so far, we have decided not to treat these types as identical.

#### Non-recombination active defects:

According to the Kveder model non-recombination active line defects at room temperature (without a defect level  $E_M$ ) exhibit an increasing recombination activity at around 130 K which is again in good agreement with our observations. Below 130 K the recombination probability via the shallow defect bands  $D_e$  and  $D_h$  becomes more

probable. Therefore it can be concluded according to Kveder *et al.* that defect structures showing no recombination activity at room temperatures are not decorated with electrically active impurities. Note that in Fig. 2(c) only the trends predicted by the Kveder model are shown. A quantitative description has to be done.

Since the trend of the temperature-dependent recombination behavior is in good agreement with the model proposed by Kveder *et al.* [15] we assume that the model is applicable for line defects. Additionally, the situation at the line defects for the different defect types can be assumed as it is described by Kveder *et al.*

## 6 SUMMARY

In this contribution we have discussed two models explaining the observed properties of the defect classification introduced in a previous publication [1]. For this we have applied detailed microscopic investigations, temperature dependent EBIC measurements and root cause analysis on an nm-scale.

It has been shown that the type-A defect structure has to be separated into type- $A_P$  (having a point-like increased recombination activity next to the grain boundary) and type- $A_G$  (having strong recombination activity and being located in between type- $A_P$  sites). It was shown that iron precipitates are responsible for the recombination and prebreakdown behavior at type- $A_P$  sites leading to a surface recombination at interface states at the interface between the metal precipitate and the silicon material. Type- $A_G$  regions most likely decorated with iron impurities can be described by the model of Kveder *et al.* [15]. Here deep defect states  $E_M$  introduced by the impurities are responsible for the recombination behavior.

According to the Kveder model and our observations the recombination processes at type-B defect structures are either due to a low impurity level or a shallower defect level  $E_M$  both explaining the observed high intensity of defect luminescence. The temperature dependency of the recombination behavior is in agreement to the Kveder model.

It was shown that on a microscopic scale a further type-C has to be introduced. It is concluded that the situation at type-C defects is similar to type- $A_G$  defect structures. Nevertheless, since the situation at type-C defects is unknown so far we will not treat these two defect types as identical. Based on these investigations the defect classification can now summarized as pictograms as shown in Table 2.

	Recombination behavior	prebreakdown behavior	defect luminescence	recombination process
	EL	ReBEL (type-2)	ELsub	Model
Type $A_P$				
Type $A_G$				
Type B				
Type C				

**Table 1:** Summary of the main properties of the defect classification as pictograms.

## 7 ACKNOWLEDGEMENT

The author would like to thank A. Hähnel and H. Blumtritt for TEM investigations and FIB preparation. M. Schütze is acknowledged for his support during preparation of this contribution. J. Bauer acknowledges the financial support by the German Federal Ministry for the Environment, Nature Conservation and Nuclear Safety and by industry partners within the research cluster “SolarWinS” (contract No. 0325270C). The authors gratefully acknowledge the financial support by the state of Saxony-Anhalt within the framework of the Leading-Edge Cluster Competition and Solarvalley Central Germany under contract No. 03IP607 (Adaptum Project).

Springer Verlag (2004)

## 8 REFERENCES

- [1] D. Lausch, K. Petter, B. Henke, R. Bakowskie, S. Schweizer, C. Hagendorf, *Energy Procedia* **8**, pp. 28-34 (2011)
- [2] K. Bothe, K. Ramspeck, D. Hinken, C. Schinke, J. Schmidt, S. Herlufsen, R. Brendel, J. Bauer, J.-M. Wagner, N. Zakharov, O. Breitenstein, *J. Appl. Phys.* **106**, 104510 (2009).
- [3] O. Breitenstein, J. Bauer, K. Bothe, W. Kwapil, D. Lausch, U. Rau, J. Schmidt, M. Schneemann, M. C. Schubert, J.-M. Wagner and W. Warta, *J. Appl. Phys.* **109**, 071101 (2011).
- [4] W. Kwapil et al., *J. Appl. Phys.* **108**, 023708 (2010)
- [5] J. Bauer, A. Hähnel, H. Blumtritt, D. Lausch, W. Kwapil, O. Breitenstein, 2AV.6.20 27st EU-PVSEC, 2012 Frankfurt
- [6] D. Lausch, R. Bakowskie, M. Lorenz, S. Schweizer, K. Petter, C. Hagendorf, *Solid State Phenomena* **178** pp. 88-93 (2011).
- [7] R. Bakowskie, R. Lantzsch, T. Kaden, K.-G. Eller, D. Lausch, Y. Ludwig, K. Petter, 26th EU-PVSEC Hamburg (2011), 2BV-4-17
- [8] D. Lausch, R. Bakowskie, H. v. Wenckstern, S. Swatek, K. Petter, C. Hagendorf, FAHL-Academiae - Defects in Semiconductors and their Characterization, Universität Leipzig (2011)
- [9] S. Johnston, F. Yan, D. Dorn, K. Zaunbrecher, M. Al-Jassim, O. Sidelkheir, and K. Ounadjela, 38th IEEE Photovoltaic Specialists Conference, 2012.
- [10] T. Fuyuki et al., Proceedings of the 20th EU-PVSEC, Barcelona (2005) p. 667
- [11] T. Trupke et al., 22nd EU-PVSEC (2007), Milan, Italy
- [12] D. Lausch, K. Petter, H. v. Wenckstern, M. Grundmann, *Phys. Status Solidi RRL* **3**, No. 2–3, 70–72 (2009)
- [13] C. Donolato in Point and Extended Defects in Semiconductors, Plenum New York, 1989 p. 225.
- [14] M. Kittler, C. Ulhaq-Bouillet, and V. Higgs, *J. Appl. Phys.* **78**, 4573 (1995)
- [15] V. Kveder, M. Kittler, W. Schröter, *Phys. Rev. B* **63**, 115208 (2001)
- [16] A. Hähnel, J. Bauer, H. Blumtritt, O. Breitenstein, D. Lausch, W. Kwapil, submitted, please contact the authors for more information
- [17] W. Shockley and W. T. Read, *Phys. Rev.* **87** 835-842 (1952)
- [18] R. N. Hall, *The Journal of Physical Chemistry* **57** 836-839 (1953)
- [19] S. Rein, Lifetime Spectroscopy: A Method of Defect Characterization in Silicon for Photovoltaic Applications,